Pergamon

Int. J. Solids Structures Vol. 35, No. 14, pp. 1489–1513, 1998

0020-7683/98 $19.00 + .00

PII: S0020-7683(97)00125-X

NUMERICAL MODELING OF STRESS INDUCED MARTENSITIC PHASE TRANSFORMATIONS IN SHAPE MEMORY ALLOYS

G. RENGARAJAN
Department of Mechanical Engineering, Texas A&M University, College Station, TX 77843-3123, U.S.A.

R. KRISHNA KUMAR
Department of Mechanical Engineering, Indian Institute of Technology, Madras 600 036, India

and

J. N. REDDY
Department of Mechanical Engineering, Texas A&M University, College Station, TX 77843-3123, U.S.A.

(*Received* 16 *January* 1996; *in revised form* 5 *May* 1997)

Abstract—Phenomenological models of shape memory behavior are based on either continuum hypothesis (macroscopic) or on volume averages over a representative volume element consisting of several grains. These constitutive models attempt to model the shape memory behavior using macro/micromechanics and thermodynamics. In general, these models share a common feature. They describe the martensitic phase transformation by a parameter representing the martensite volume fraction, and formulate an evolution law for the martensite volume fraction. Exploiting the similarity of these models to elastoplasticity, we describe a finite element formulation of a micromechanics based constitutive model. Several other models can be formulated in a similar way, and the present work can be seen as a testbed approach to study and evaluate the constitutive models on a common platform. We present numerical results for Au-47.5at%Cd and Ti-50.6at%Ni to validate the finite element formulation. © 1998 Elsevier Science Ltd.

1. INTRODUCTION

The metallurgical underpinnings of shape memory behavior are now well understood, and the research has been documented extensively in the literature for various alloy systems that undergo reversible martensitic transformations [see Warlimont and Delaey (1974); Otsuka and Shimuzu (1986); Funakubo (1987)]. In the last decade, interest has risen in the mechanics community in constitutive modeling of these alloys, largely due to the growing applications of shape memory alloys, in particular, in the area of active material systems. The growing applications demand an *a priori* estimate of the life of the alloy, recoverability, fracture and fatigue properties, etc. A phenomenological constitutive model is a fundamental prerequisite in successfully (reasonably) answering these questions. However, the complexity of the martensitic transformation, displaying fine microstructure, poses a formidable problem in constitutive modeling.

An alloy undergoing martensitic transformation displays interesting features at multiple length scales. At the lowest length scale, the atomic/crystallographic scale ($\sim 10^{-9}$ m), we observe the crystallographic transformations from a higher symmetry crystal structure (austenite) to multiple variants of lower symmetry crystal structure (martensite). The crystallographic transformation has been studied geometrically [see Wechsler *et al.* (1953); Wayman (1964)]. Recently, atomistic methods have been used to study the phase transformations in Ti–Ni (van Midden, 1994), and attempts have been made to develop interatomic potentials for Ti and Ti–Ni.

The next length scale (moving up the ladder) is the microscopic level ($\sim 10^{-6}$ m). We look inside a grain and observe the fine microstructure of martensite, the interfaces: interface between austenite and martensite, interfaces between variants of martensite, etc. Khachaturyan (1983), and Ball and James (1987, 1992) have used energy minimization approaches to predict the formation of microstructure, the orientation of the interfaces, etc. The next length scale ($\sim 10^{-5}$ m) spans the mesoscopic to microscopic level. This length scale in itself does not exhibit significant features, but is amenable to a micromechanics treatment of the shape memory behavior. A representative volume element is considered, and martensite is treated as inclusion in the RVE. A few models have been developed using micromechanics [for e.g. Patoor *et al.* (1988; 1995); Sun and Hwang (1993); Sun *et al.* (1994)].

This leads to the final length scale ($\sim 10^{-2}$ m) which is the macroscopic length scale. The above-mentioned microstructural features manifest as the shape memory behavior, and the global cyclic stress–strain behavior is characterized by hysteresis. Continuum models of shape memory alloys at a macroscopic level include the variations of Tanaka's (1986) approach.

Other continuum models of shape memory behavior include the thermodynamic models (Müller, 1994; Raniecki and Lexcellent, 1994; Boyd and Lagoudas, 1994), the study of nucleation and growth of martensites and the study of interface transport (interface between austenite and martensite) by Abeyaratne *et al.* (1994; 1995). There are several other models, but these models are in general similar in some respects to the models mentioned above.

In the realm of phenomenological modeling, the micromechanical-based approaches offer a reasonable level of sophistication. The key aspect of these models is the number of independent material parameters that need to be determined experimentally. Sometimes, these models are quite sensitive to variations in a few of these parameters. The success of the constitutive model depends largely on the accuracy to which we can specify these parameters for a given material. In general, these parameters can be determined from simple uniaxial tensile-compressive loading experiments [see Miyazaki *et al.* (1981)], calorimetric measurements [see Salzbrenner and Cohen (1979)], and acoustic emission techniques (Baram and Rosen, 1982). However, the alloy composition differs by a few percentage from one group to another, even for the same alloy system. While minor variations in composition do not affect material properties significantly, it does affect the transformation temperature drastically (Hasiguti and Iwasaki, 1968). We will address this issue further in the numerical results section of the paper.

In order to estimate the range of applicability of these models, under varying conditions, it is necessary to study them from a unified standpoint. A numerical approach, such as the finite element method, offers a testbed approach to evaluate these constitutive models against one another, and with experimental results (Krishnakumar *et al.*, 1995). Brinson and Lammering (1992) were perhaps the first to present a finite element formulation for the analysis of the shape memory behavior. They presented a nonlinear formulation based on a modified form of Tanaka's (1986) model. Bo and Lagoudas (1994) have implemented a few continuum models from literature into a finite element program and have compared these models. They have also used the operator split method of Ortiz and Simo (1986) to integrate the constitutive equations.

Our purpose in this paper is two-fold. First, we wish to show the strong resemblance of the micromechanics based models to elastoplasticity, and hence, the ease with which these models can be implemented in a standard elastoplastic finite element code. The finite element implementation of the constitutive models will provide a testbed for evaluating several constitutive models. Towards this purpose, we present a finite element formulation of a micromechanics based constitutive model (Sun and Hwang, 1993; Sun *et al.*, 1994). Secondly, we make an attempt to model some of the uniaxial experimental data available in the literature for two alloy systems (Au-47.5at%Cd and Ti-50.6at%Ni). The problems can be solved analytically and, hence, serve as tests for the finite element solution. Also, we perform a numerical study of a thick cylinder using one of the materials mentioned above, and propose a simple approach to model *subloops* in the superelastic response of shape memory alloys.

The rest of the paper is organized as follows. We first describe the constitutive model briefly with the assumptions involved. We then describe the finite element formulation, and provide a description of the stress-update procedure. Finally, we present numerical results, and close the paper with a few remarks.

2. THE CONSTITUTIVE MODEL

We present a review of the constitutive model. Our notations are similar to the ones followed in Gurtin (1981): e.g. $[\mathbf{a} \otimes \mathbf{b}]_{ij} = a_i b_j$; $(\mathbf{a} \cdot \mathbf{b}) = a_i b_i$; $(\mathbf{A} \cdot \mathbf{B}) = A_{ij} B_{ji}$; $[\mathbf{AB}]_{ij} = A_{ik} B_{kj}$; $[\mathrm{D}[\mathbf{A}]]_{ij} = D_{ijkl} A_{kl}$.

2.1. *The representative volume element*

A representative volume element, identified with each continuum point, is chosen such that it consists of several grains. In a finite element discretization of the continuum, each Gauss quadrature point naturally corresponds to a representative volume element. The macroscopic stress, $\mathbf{S}$, and the macroscopic strain, $\mathbf{E}$, are obtained by volume averages over the RVE. The macroscopic deviatoric stress is denoted as $\mathbf{S}_\mathrm{D}$. The RVE, at a typical temperature θ and stress $\mathbf{S}$, will exhibit a microstructure that is pure *austenite* (matrix or parent), or pure *martensite* (inclusion or product), or a combination of both. The matrix transformation stress is denoted as $\boldsymbol{\sigma}$, and the transformation strain in the inclusion is denoted as $\mathbf{e}^\mathrm{p}$. The matrix transformation stress is related to the macroscopic deviatoric stress through (Mori and Tanaka, 1973; Sun and Hwang, 1993)

$$\boldsymbol{\sigma} = \mathbf{S}_\mathrm{D} - \boldsymbol{\beta}, \tag{1}$$

where the *back stress* $\boldsymbol{\beta}$, similar to kinematic hardening in classical elastoplasticity, is given by

$$\boldsymbol{\beta} = f B(\theta)\, \boldsymbol{\varepsilon}^\mathrm{p}. \tag{2}$$

In the above equation, f is the martensite volume fraction over the RVE, $\boldsymbol{\varepsilon}^\mathrm{p}$ is the volume average strain over the inclusions in the RVE,

$$\boldsymbol{\varepsilon}^\mathrm{p} = \langle \mathbf{e}^\mathrm{p} \rangle_{V_\mathrm{I}},$$

and $B(\theta)$ is a temperature dependent material parameter that is related to shear modulus $\mu(\theta)$ and Poisson's ratio ν through

$$B(\theta) = \frac{2\mu(\theta)(5\nu - 7)}{15(1-\nu)}. \tag{3}$$

Note that the shape of the inclusions have been assumed to be spheroids in the micromechanics derivation using the Mori–Tanaka theory. Similar micromechanics based approaches can also be found in Patoor *et al.* (1988), and Boyd and Lagoudas (1996).

The strains are decomposed as

$$\dot{\mathbf{E}} = \dot{\mathbf{E}}^\mathrm{e} + \dot{\mathbf{E}}^\mathrm{p} \tag{4}$$

where

$$\dot{\mathbf{E}}^\mathrm{e} = \mathbf{M}[\dot{\mathbf{S}}] \tag{5}$$

is the elastic strain, $\mathbf{M}$ is the elastic compliance tensor, and

$$\dot{\mathbf{E}}^{\mathrm{p}} = \dot{\overline{f\boldsymbol{\varepsilon}^{\mathrm{p}}}} = \dot{f}\boldsymbol{\varepsilon}^{\mathrm{p}} \tag{6}$$

is the volume averaged transformation strain. The transformation in each grain has been assumed to be completed instantaneously, and the state of all the grains that have undergone transformation prior to the current transformation remains unchanged. Hence, $\dot{\boldsymbol{\varepsilon}}^{\mathrm{p}} = 0$.

The transformation strain is assumed to be (Sun and Hwang, 1993)

$$\boldsymbol{\varepsilon}^{\mathrm{p}} = \frac{\sqrt{3}}{2}\gamma\frac{\boldsymbol{\sigma}}{\sigma_{\mathrm{e}}}, \tag{7}$$

where the strain constant γ is given by

$$\gamma = \sqrt{3}\mathbf{e}_{\mathrm{e}}^{\mathrm{p}}, \quad \mathbf{e}_{\mathrm{e}}^{\mathrm{p}} = (\tfrac{2}{3}\mathbf{e}^{\mathrm{p}}\cdot\mathbf{e}^{\mathrm{p}})^{1/2}, \tag{8}$$

but is assumed to be a material constant, and the equivalent stress σ_{e} is given by

$$\sigma_{\mathrm{e}} = (\tfrac{3}{2}\boldsymbol{\sigma}\cdot\boldsymbol{\sigma})^{1/2}. \tag{9}$$

Equation (7) has been postulated under the assumption that the transformation strain in each grain is either along or parallel to the average matrix stress $\boldsymbol{\sigma}$. We know that the martensite variant that is aligned favorably to the external load grows at the expense of other variants, and this observation supports the approximation in eqn (7).

2.2. *The free energy*

The Helmholtz free energy density is given by [cf. Sun and Hwang (1993); Raniecki and Lexcellent (1994); Fischer *et al.* (1994); Boyd and Lagoudas (1996)]

$$\rho\psi = \hat{\psi}(\mathbf{E}, \theta, f, \boldsymbol{\varepsilon}^{\mathrm{p}}) = \psi_{\mathrm{el}} + \psi_{\mathrm{int}} + \psi_{\mathrm{ch}}. \tag{10}$$

The elastic energy density ψ_{el} is given by

$$\psi_{\mathrm{el}} = \psi_{\mathrm{el}}^{1} + \psi_{\mathrm{el}}^{2}, \tag{11}$$

where ψ_{el}^{1} is the linear elastic strain energy due to the macroscopic stress and strain,

$$\psi_{\mathrm{el}}^{1} = \tfrac{1}{2}\mathbf{S}\cdot\mathbf{E}^{\mathrm{e}} = \tfrac{1}{2}\mathbf{S}\cdot\mathbf{M}[\mathbf{S}],$$

and ψ_{el}^{2} is the elastic strain energy due to internal transformation and self-accommodation,

$$\psi_{\mathrm{el}}^{2} = \tfrac{1}{2}B(\theta)f^{2}\boldsymbol{\varepsilon}^{\mathrm{p}}\cdot\boldsymbol{\varepsilon}^{\mathrm{p}} - \tfrac{1}{4}B(\theta)\gamma^{2}f.$$

The above equation is similar in structure to eqn (16) of Raniecki and Lexcellent (1994) and eqn (54) of Boyd and Lagoudas (1996).

The interfacial energy density ψ_{int} is taken to be

$$\psi_{\mathrm{int}} = H(\theta)f(1-f), \tag{12}$$

which is based on the fact that the interfacial energy is zero in both the pure austenite phase ($f = 0$) and the pure martensite phase ($f = 1$), and is assumed to be a maximum at $f = 1/2$. See Müller and Xu (1991) for the interpretation of a similar expression for interface energy, and its relation to hysteresis observed in the cyclic loadings [see Sun *et al.* (1994)]. Note that while we have assumed the above form for interfacial energy (12) in the present paper,

extensions or modifications to accommodate other forms of interfacial energy can be accomplished easily. We will see later that $-H(\theta)$ in (12) represents behavior similar to isotropic hardening in classical plasticity.

The chemical free energy density is assumed to be of the form

$$\psi_{ch}(\theta, f) = \Delta G(\theta) f \tag{13}$$

and

$$\Delta G(\theta) = k(\theta - \theta_0) \tag{14}$$

where θ_0 is the transformation temperature, and k is a material constant that is representative of the entropy change per unit volume at transformation temperature [see the Clausius–Clapeyron equation, Wollants *et al.* (1993)].

2.2.1. *Remark* 1. The transformation temperature is often assumed to lie between M_s and A_f, and hence, it is usual to set $\theta_0 = 1/2\ (M_s + A_f)$ (M_s denotes martensite start temperature, and A_f denotes austenite finish temperature). However, Salzbrenner and Cohen (1979) show that this assumption is valid for single crystal, multiple interface transformation where the first martensite plate nucleates at M_s (at the crystal free edge), and the last plate to revert back to the parent phase is at A_f. However, this assumption is not strictly valid in polycrystalline specimens and few special morphologies of single crystals [see Ortin and Planes (1988)].

We have not included the thermal contributions due to structural heating in the free energy density since our study is going to be restricted to isothermal stress-induced transformations in this paper. In a sequel, we will include all the relevant thermal terms to the free energy (as it should be done), and present the resulting model and the numerical formulation.

Finally, the energy dissipated during the transformation has been assumed to be

$$\mathscr{D} = \begin{cases} D_0 \dot{f} & \text{(forward transformation)} \\ -D_0 \dot{f} & \text{(reverse transformation)} \end{cases} \tag{15}$$

where D_0 is a material dissipation constant. The complementary free energy density is given by (Rice, 1971)

$$\hat{\phi}(\mathbf{S}, \theta, f, \boldsymbol{\varepsilon}^p) = -(\hat{\psi} - \mathbf{S} \cdot \mathbf{E}). \tag{16}$$

Substituting eqns (11)–(13) in the complementary free energy density (16), we obtain

$$\hat{\phi}(\mathbf{S}, \theta, f, \boldsymbol{\varepsilon}^p) = \tfrac{1}{2}\mathbf{S} \cdot \mathbf{M}[\mathbf{S}] + f\mathbf{S} \cdot \boldsymbol{\varepsilon}^p - H(\theta) f(1-f) - \Delta G(\theta) f + \tfrac{1}{4} B(\theta) \gamma^2 f - \tfrac{1}{2} B(\theta) f^2 \boldsymbol{\varepsilon}^p \cdot \boldsymbol{\varepsilon}^p. \tag{17}$$

2.3. *Summary of assumptions in the constitutive model*

The constitutive model has been developed with the following assumptions and limitations:

(1) Only the long range effects of the transformation process are considered; the microstructural or atomistic level changes are not accounted for.

(2) Thermal expansion difference between the martensite and parent phases are neglected.

(3) The grains are assumed to be equi-sized, and all grains are assumed to have equal probability for nucleation.

(4) The total energy dissipated during the transformation is assumed to be proportional to the volume fraction of the transformation.

(5) The shape of the martensite inclusions is assumed to be spheroidal.

(6) The transformation in each grain is assumed to be accomplished instantaneously, and the state of all the grains that transformed prior to the current transformation is assumed to remain unchanged. The transformation strain can vary from inclusion to inclusion, but is taken to be uniform within an inclusion.

(7) At the instant of transformation, the transformation strain is either along or parallel to the average stress $\boldsymbol{\sigma}$.

2.4. *The transformation condition and evolution equation*

The transformation condition can be derived using the thermodynamic framework [for e.g. Ziegler (1987)], by equating $\hat{\phi}|_{S,\theta} = \mathscr{D}$, that is,

$$-\frac{\partial \hat{\phi}}{\partial f}\dot{f} = \mathscr{D}.$$

The transformation conditions are obtained as

2.4.1. *Forward transformation* ($p \rightarrow m$).

$$T_f = \frac{\gamma}{\sqrt{3}}\sigma_e - C_f(\theta,f) = 0. \tag{18}$$

2.4.2. *Reverse transformation* ($m \rightarrow p$).

$$T_r = \frac{\gamma}{\sqrt{3}}\sigma_e - C_r(\theta,f) = 0, \tag{19}$$

where

$$C_f(\theta,f) = -\tfrac{1}{4}B(\theta)\gamma^2 + H(\theta)(1-2f) + \Delta G(\theta) + D_0. \tag{20}$$

As mentioned earlier, the second term in eqn (20), $-2H(\theta)f$, represents linear hardening similar to isotropic hardening. Also, for the reverse transformation,

$$C_r(\theta,f) = C_f(\theta,f) - 2D_0. \tag{21}$$

The parameters $C_f(\theta,f)$ and $C_r(\theta,f)$ at $f = 0$ represent the equivalent stress required to initiate the forward and reverse transformations, respectively. These parameters carry the hardening information [$H(\theta)$], and are similar to the yield stress in elastoplasticity.

The evolution equation for the martensite volume fraction during the forward transformation is obtained by setting $\dot{T}_f = 0$, and is given by

$$\dot{f} = \frac{\dfrac{\partial T_f}{\partial \mathbf{S}}\cdot\dot{\mathbf{S}} + \dfrac{\partial T_f}{\partial \theta}\dot{\theta}}{-\dfrac{\partial T_f}{\partial f}}, \tag{22}$$

with

$$-\frac{\partial T_f}{\partial f} > 0. \tag{23}$$

Using eqn (18) in eqn (22), we obtain

$$\dot{f} = \frac{1}{F(\theta)} \{\boldsymbol{\varepsilon}^{\mathrm{p}} \cdot \dot{\mathbf{S}} - P(\theta, f)\dot{\theta}\} \tag{24}$$

where

$$F(\theta) = \frac{\gamma^2}{2} B(\theta) - 2H(\theta), \tag{25}$$

and

$$P(\theta, f) = \frac{\mathrm{d}B}{\mathrm{d}\theta} f \boldsymbol{\varepsilon}^{\mathrm{p}} \cdot \boldsymbol{\varepsilon}^{\mathrm{p}} + \frac{\partial C_{\mathrm{f}}}{\partial \theta}. \tag{26}$$

In numerical simulation, the condition $\dot{T}_{\mathrm{f}} = 0$ will also serve as a consistency condition. Similarly, $\dot{T}_{\mathrm{r}} = 0$ yields the consistency condition for the reverse transformation. Also, the structure of transformation conditions (18) and (19) and evolution eqn (24) are similar to the corresponding equations in Patoor *et al.* (1988), and Boyd and Lagoudas (1996).

2.4.3. *Remark* 2. In contrast to elastoplasticity, where we have elastic unloading, the superelastic behavior of shape memory alloys is characterized by elastic unloading and a reverse yield like behavior that corresponds to the reverse transformation.

2.5. *Stress–strain relations*

In this paper, the focus is on isothermal behavior of shape memory alloys, and hence $\dot{\theta} = 0$. Therefore, the evolution equation (24) reduces to

$$\dot{f} = \frac{1}{F} \boldsymbol{\varepsilon}^{\mathrm{p}} \cdot \dot{\mathbf{S}}. \tag{27}$$

The incremental stress–strain relations are

$$\dot{\mathbf{E}} = \mathbf{M}[\dot{\mathbf{S}}] + \boldsymbol{\varepsilon}^{\mathrm{p}} \dot{f}. \tag{28}$$

Substituting eqn (27) in the above equation, we obtain

$$\dot{\mathbf{E}} = \mathbf{M}_{\mathrm{g}}[\dot{\mathbf{S}}] \tag{29}$$

where

$$\mathbf{M}_{\mathrm{g}} = \mathbf{M} + \frac{1}{F} \boldsymbol{\varepsilon}^{\mathrm{p}} \otimes \boldsymbol{\varepsilon}^{\mathrm{p}}. \tag{30}$$

The constitutive model is summarized in Table 1.

3. FINITE ELEMENT FORMULATION

The formulation is in general similar to small strain, rate independent elastoplastic formulations [see Simo and Hughes (1988)]. Let Ω be a sufficiently smooth domain, and $\partial\Omega$ be the boundary of the domain.

3.1. *Weak form and linearization of the momentum balance equation*

Given a general nonlinear functional $R = R(\mathbf{u})$, we can linearize R about a particular configuration $\bar{\mathbf{u}}$ (Gurtin, 1981) as

Table 1. Summary of the constitutive model

Stress–strain relations

$$\dot{\mathbf{E}} = \dot{\mathbf{E}}^{\mathrm{e}} + \dot{\mathbf{E}}^{\mathrm{p}}$$
$$\dot{\mathbf{E}}^{\mathrm{e}} = \mathbf{M}[\dot{\mathbf{S}}]$$
$$\dot{\mathbf{E}}^{\mathrm{p}} = \dot{f}\boldsymbol{\varepsilon}^{\mathrm{p}}$$
$$\boldsymbol{\varepsilon}^{\mathrm{p}} = \frac{\sqrt{3}}{2}\gamma\frac{\boldsymbol{\sigma}}{\sigma_{\mathrm{e}}}.$$

Transformation conditions

$$T_{\mathrm{f}} = \frac{\gamma}{\sqrt{3}}\sigma_{\mathrm{e}} - C_{\mathrm{f}}(\theta, f) = 0 \quad \text{(Forward)}$$
$$T_{\mathrm{r}} = \frac{\gamma}{\sqrt{3}}\sigma_{\mathrm{e}} - C_{\mathrm{r}}(\theta, f) = 0 \quad \text{(Reverse)}.$$

Evolution equation

$$\dot{f} = \frac{1}{F(\theta)}\{\boldsymbol{\varepsilon}^{\mathrm{p}} \cdot \mathbf{S} - P(\theta, f)\dot{\theta}\}$$
$$F(\theta) = \frac{\gamma^2}{2}B(\theta) - 2H(\theta) > 0$$
$$P(\theta, f) = \frac{\mathrm{d}B}{\mathrm{d}\theta}f\boldsymbol{\varepsilon}^{\mathrm{p}} \cdot \boldsymbol{\varepsilon}^{\mathrm{p}} + \frac{\partial C_{\mathrm{f}}}{\partial \theta}.$$

$$\mathscr{L}[R(\mathbf{u})]_{\mathbf{0}} = R(\bar{\mathbf{u}}) + DR(\mathbf{u})[\Delta\mathbf{u}] = 0, \tag{31}$$

where

$$DR(\mathbf{u})[\Delta\mathbf{u}] = \frac{d}{d\alpha}[R(\bar{\mathbf{u}} + \alpha\Delta\mathbf{u})]_{\alpha=0}. \tag{32}$$

In general, we use Newton class of algorithms to solve the resulting equations.

We shall assume that the deformations are quasi-static and, hence, neglect inertial effects, and further neglect body forces also. The weak form of the momentum balance ($\mathrm{div}\,\mathbf{S} = 0$) can be written as

$$R(\mathbf{u}, \delta\mathbf{u}) = \int_{\Omega} \mathbf{S} \cdot \nabla\delta\mathbf{u}\,\mathrm{d}V - \int_{\partial\Omega} (\mathbf{Sn}) \cdot \delta\mathbf{u}\,\mathrm{d}S = 0. \tag{33}$$

Linearizing the above equation about $\bar{\mathbf{u}}$, we get

$$B(\Delta\mathbf{u}, \delta\mathbf{u}) = \ell(\delta\mathbf{u}) - \bar{R}(\bar{\mathbf{u}}, \delta\mathbf{u}), \tag{34}$$

where

$$B(\Delta\mathbf{u}, \delta\mathbf{u}) = \int_{\Omega} \nabla\delta\mathbf{u} \cdot \mathbf{M}_{\mathrm{g}}^{-1}[\delta\mathbf{E}]\,\mathrm{d}V,$$
$$\ell(\delta\mathbf{u}) = \int_{\partial\Omega} \delta\mathbf{u} \cdot \hat{\mathbf{t}}\,\mathrm{d}S,$$
$$\bar{R}(\bar{\mathbf{u}}, \delta\mathbf{u}) = \int_{\Omega} \nabla\delta\mathbf{u} \cdot \bar{\mathbf{S}}\,\mathrm{d}V,$$

and $\hat{\mathbf{t}} = \mathbf{Sn}$ is the applied traction on a part of the boundary.

3.2. *Matrix formulation*

We have assumed small strains†. The strains are related to displacements as

$$\mathbf{E} = \tfrac{1}{2}(\nabla\mathbf{u} + (\nabla\mathbf{u})^{\mathrm{T}}) =: \mathbf{B}\mathbf{u}, \tag{35}$$

where $\mathbf{B}$ is the gradient operator matrix. Let the computational domain be discretized in to N elements such that

$$\Omega = \bigoplus_{e=1}^{N} \Omega_e.$$

where $\oplus$ denotes the direct sum, and Ω_e denotes the element space. We interpolate the displacements at the element level as

$$\mathbf{u}_e = \sum_{a=1}^{NEN} \mathbf{N}_a \mathbf{d}^a, \tag{36}$$

and the trial functions as

$$\delta\mathbf{u}_e = \sum_{a=1}^{NEN} \delta\mathbf{d}^{a\mathrm{T}} \mathbf{N}_a^{\mathrm{T}}, \tag{37}$$

where $\mathbf{N}^a$ are the shape functions, $\mathbf{d}^a$ are the nodal unknowns, and NEN denotes the number of nodes per element. For a given node a in the element, $\mathbf{d}^a$ and $\delta\mathbf{d}^a$ will have as many components as number of degrees-of-freedom per node in the element. We can write eqns (36) and (37) as

$$\mathbf{u}_e = \mathbf{N}\mathbf{d} \quad \delta\mathbf{u}_e = \delta\mathbf{d}^{\mathrm{T}}\mathbf{N}^{\mathrm{T}} \tag{38}$$

where

$$\mathbf{d} = [\mathbf{d}_1 \mathbf{d}_2 \ldots \mathbf{d}_{NEN}]^{\mathrm{T}}$$

$$\delta\mathbf{d} = [\delta\mathbf{d}_1 \delta\mathbf{d}_2 \ldots \delta\mathbf{d}_{NEN}]^{\mathrm{T}},$$

and $\mathbf{N}$ is an appropriate matrix form of the shape functions depending on the type of element. We have

$$\mathbf{E}_e = \mathbf{B}\mathbf{u}_e = \mathbf{B}_{\mathrm{N}}\mathbf{d} \tag{39}$$

where‡ $\mathbf{B}_{\mathrm{N}} = \mathbf{B}\mathbf{N}$ (in element natural coordinates). Further, $\Delta\mathbf{u} = \mathbf{N}\,\Delta\mathbf{d}$.

We now divide the total time $[0, t]$ into M time intervals $[t_n, t_{n+1}]$, such that

$$[0, t] = \bigoplus_{n=0}^{M-1} [t_n, t_{n+1}].$$

At a given time step, t_{n+1} ($t_{n+1} = t_n + \Delta t$) all the variables at time step t_n ($\mathbf{S}_n, \mathbf{E}_n, f_n, \boldsymbol{\sigma}_n, \boldsymbol{\varepsilon}_n^{\mathrm{p}}$) are known. Making the substitutions (36)–(39) in the weak form (34), we can obtain the discretized weak form of the momentum balance as

† The shape memory alloys are capable of being strained up to 2–8%. This apparently plastic, large deformation is mostly recoverable, and hence, a small strain assumption is reasonable as long as the application does not involve finite rotations.

‡ Note that $\mathbf{E}_e$ is the total strain in an element, and this should not be confused with the elastic strain $\mathbf{E}^e$.

$$B_e^h(\Delta \mathbf{d}_{n+1}, \delta \mathbf{d}) = \ell_e^h(\delta \mathbf{d}) - \langle \mathbf{S}_{n+1}, \delta \mathbf{d} \rangle, \tag{40}$$

where

$$B_e^h(\Delta \mathbf{d}_{n+1}, \delta \mathbf{d}) = \int_{\Omega_e} \delta \mathbf{d}^T \mathbf{B}_N^T \mathbf{M}_g^{-1} \mathbf{B}_N \Delta \mathbf{d} \, dV,$$

$$\ell_e^h(\delta \mathbf{d}) = \int_{\partial \Omega_e} \delta \mathbf{d}^T \mathbf{N}^T \hat{\mathbf{t}} \, dS,$$

$$\langle \mathbf{S}_{n+1}, \delta \mathbf{d} \rangle = \int_{\Omega_e} \delta \mathbf{d}^T \mathbf{B}_N^T \mathbf{S}_{n+1} \, dV.$$

After assembly, at t_{n+1}, we can write the above equation as

$$\delta \mathbf{d}^T \mathbf{K}_T \Delta \mathbf{d}_{n+1} = \delta \mathbf{d}^T \mathbf{R}_{n+1} \tag{41}$$

where the tangent stiffness matrix is given by

$$\mathbf{K}_T = \bigcup_{e=1}^{N} \int_{\Omega_e} \mathbf{B}_N^T \mathbf{M}_g^{-1} \mathbf{B}_N \, dV,$$

and the right-hand side vector $\mathbf{R}$ is given by

$$\mathbf{R}_{n+1} = \bigcup_{e=1}^{N} \left[-\int_{\Omega_e} \mathbf{B}_N^T \mathbf{S}_{n+1} \, dV + \int_{\partial \Omega_e} \mathbf{N}^T \hat{\mathbf{t}} \, dS \right]. \tag{42}$$

3.3. *Integration of constitutive equations*

A two-step algorithm based on the elastic–plastic operator split technique (Ortiz and Simo, 1986) is used to integrate the constitutive equations (Table 1). The operator split technique is based on additive decomposition of the constitutive equations into an elastic predictor part

$$\begin{aligned} &\dot{\mathbf{E}} = \dot{\mathbf{E}}^e, \quad \dot{\mathbf{E}}^p = 0, \\ &\dot{\mathbf{S}} = \mathbf{M}^{-1}[\dot{\mathbf{E}}^e], \\ &\dot{f} = 0, \end{aligned} \tag{43}$$

and a plastic corrector part

$$\begin{aligned} &\dot{\mathbf{E}} = \dot{\mathbf{E}}^e + \dot{\mathbf{E}}^p = 0, \\ &\dot{\mathbf{S}} = -\dot{f}\mathbf{M}^{-1}[\boldsymbol{\varepsilon}^p], \\ &\dot{f} = \dot{f}(\dot{\mathbf{S}}). \end{aligned} \tag{44}$$

The transformation condition (T_f) can be linearized at the current time as

$$T_{f(n+1)}^{(i+1)} = T_{f(n+1)}^{(i)} + \frac{\partial T_f}{\partial \mathbf{S}} \cdot \Delta \mathbf{S} + \frac{\partial T_f}{\partial f} \Delta f = 0. \tag{45}$$

Note that $\dot{\boldsymbol{\varepsilon}}^p = 0$. We have

Table 2. Stress update algorithm

Step I. Update strains

$\mathbf{u}_{n+1} = \mathbf{u}_n + \Delta\mathbf{u}_{n+1}$

$\mathbf{E}_{n+1} = \mathbf{E}_n + \mathbf{B}\mathbf{u}_{n+1}$.

Step II. Elastic predictor

$\mathbf{E}^{p(0)}_{n+1} = \mathbf{E}^p_n$

$\mathbf{E}^{e(0)}_{n+1} = \mathbf{E}_{n+1} - \mathbf{E}^{p(0)}_{n+1}$

$\mathbf{S}^0_{n+1} = \mathbf{M}^{-1}[\mathbf{E}^{e(0)}_{n+1}]$

$f^0_{n+1} = f_n$

$\boldsymbol{\varepsilon}^{p(0)}_{n+1} = \boldsymbol{\varepsilon}^p_n$

Step III. Check for transformation

IF $T^{(0)}_{f(n+1)} \leqslant 0$ THEN

$\mathbf{E}^p_{n+1} = \mathbf{E}^{p(0)}_{n+1}$, $\mathbf{E}^e_{n+1} = \mathbf{E}^{e(0)}_{n+1}$, $\mathbf{S}_{n+1} = \mathbf{S}^0_{n+1}$

$f_{n+1} = f^0_{n+1}$, $\boldsymbol{\varepsilon}^p_{n+1} = \boldsymbol{\varepsilon}^{p(0)}_{n+1}$, EXIT.

ELSE $i = 0$, GO TO Step IV.

Step IV. Plastic correctors

$$\Delta f = \frac{T^{(i)}_{f(n+1)}}{\mathbf{t}^{p(i)}_{(n+1)} \cdot M^{-1}[\boldsymbol{\varepsilon}^{p(i)}_{(n+1)}] + F(\theta)}$$

$\mathbf{S}^{(i+1)}_{(n+1)} = \mathbf{S}^{(i)}_{(n+1)} - \Delta f \mathbf{M}^{-1}[\boldsymbol{\varepsilon}^{p(i)}_{(n+1)}]$

$f^{(i+1)}_{(n+1)} = f^{(i)}_{(n+1)} + \Delta f$

$\boldsymbol{\varepsilon}^{p(i+1)}_{(n+1)} = \boldsymbol{\varepsilon}^p(\boldsymbol{\sigma}^{(i+1)}_{(n+1)})$.

Step V. Check for convergence

IF $|T^{(i+1)}_{f(n+1)}| \leqslant \mathrm{TOL}\,|T^0_{f(n+1)}|$ THEN

$\mathbf{S}_{n+1} = \mathbf{S}^{(i+1)}_{(n+1)}$, $f_{n+1} = f^{(i+1)}_{(n+1)}$

$\mathbf{E}^e_{n+1} = \mathbf{E}^e(\mathbf{S}_{n+1}, f_{n+1})$, $\mathbf{E}^p_{n+1} = \mathbf{E}_{n+1} - \mathbf{E}^e_{n+1}$

ELSE

$i \leftarrow i+1$, GO TO Step IV.

$$\frac{\partial T_f}{\partial \mathbf{S}} = \boldsymbol{\varepsilon}^{\mathrm{p}} \tag{46}$$

and

$$\frac{\partial T_f}{\partial f} = -F(\theta). \tag{47}$$

Substituting eqns (46) and (47) in eqn (45), we can solve for Δf, to obtain

$$\Delta f = \frac{T^{(i)}_{f(n+1)}}{\boldsymbol{\varepsilon}^{\mathrm{p}} \cdot \mathbf{M}^{-1}[\boldsymbol{\varepsilon}^{\mathrm{p}}] + F(\theta)}. \tag{48}$$

The procedure is quite similar for reverse transformation. The stress update algorithm is summarized in Table 2.

4. NUMERICAL RESULTS

To validate the finite element formulation presented in the last section, we consider two alloy systems, Au-47.5at%Cd and Ti-50.6at%Ni. Analytical solutions are possible under simple proportional loading schemes, and specifically we study the stress–strain behavior of these alloys under a uniaxial stress state. Following this, we model an infinitely long thick cylinder made of Au-47.5at%Cd, and study its transformation behavior.

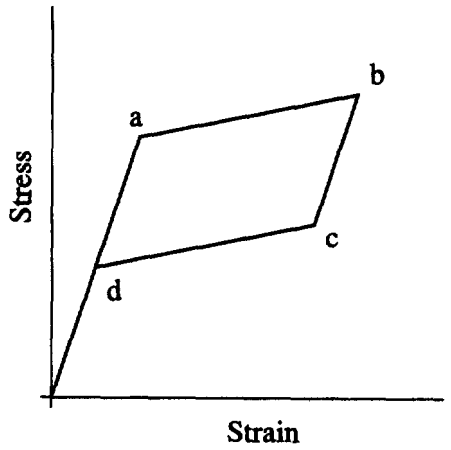

Fig. 1. An idealized uniaxial stress–strain curve with transformation points: (a) $f = 0$, $p \to m$; (b) $f = 1$, $p \to m$; (c) $f = 1$, $m \to p$; (d) $f = 0$, $m \to p$.

4.1. *Proportional loading*

Under proportional loading, we have

$$\mathbf{S} = \bar{\boldsymbol{\lambda}} S_e \tag{49}$$

where $\bar{\boldsymbol{\lambda}}$ is the load proportionality constant (a tensor here), S_e is the equivalent stress. It is easy to see that the deviatoric stress can be written as

$$\mathbf{S}_D = \boldsymbol{\lambda} S_e$$

where $\boldsymbol{\lambda}$ is related to $\bar{\boldsymbol{\lambda}}$ and an hydrostatic component, and we have

$$\boldsymbol{\sigma} = \boldsymbol{\lambda} \sigma_e \tag{50}$$

and

$$S_e = \sigma_e + \frac{\sqrt{3}}{2} f B(\theta) \gamma.$$

Therefore, the transformation strain can now be written as

$$\boldsymbol{\varepsilon}^p = \frac{\sqrt{3}}{2} \gamma \boldsymbol{\lambda} = \frac{\sqrt{3}}{2} \gamma \frac{\mathbf{S}_D}{S_e}. \tag{51}$$

The transformation conditions reduce to

$$\frac{\gamma}{\sqrt{3}} S_e - \frac{\gamma^2}{2} f B(\theta) - C_f(\theta, f) = 0 \quad \text{(Forward, } p \to m\text{)}.$$

$$\frac{\gamma}{\sqrt{3}} S_e - \frac{\gamma^2}{2} f B(\theta) - C_r(\theta, f) = 0 \quad \text{(Reverse, } m \to p\text{)}. \tag{52}$$

4.1.1. *Uniaxial stress state.* Consider a uniaxial stress state such that $S_e = S_{11}$. The stress–strain relations (29) reduce to

$$\dot{E}_{11} = \left[\frac{1}{E} + \frac{\gamma^2}{3F(\theta)} \right] \dot{S}_{11}. \tag{53}$$

A typical uniaxial stress–strain response with linear hardening behavior is shown in Fig. 1.

For the linear hardening behavior, it is easy to estimate analytically the stresses at points marked a, b, c, d in the figure. These are given by [using eqn (52)]

$$S^1 = S_{11}|_a = \frac{\sqrt{3}}{\gamma} C_f,$$

$$S^2 = S_{11}|_b = \frac{\sqrt{3}}{\gamma}\left(\frac{\gamma^2}{2} B(\theta) + C_f(\theta) - 2H(\theta)\right),$$

$$S^3 = S_{11}|_c = \frac{\sqrt{3}}{\gamma}\left(\frac{\gamma^2}{2} B(\theta) + C_r(\theta) - 2H(\theta)\right),$$

$$S^4 = S_{11}|_d = \frac{\sqrt{3}}{\gamma} C_r.$$

If we define the width of the hysteresis loop (h) as

$$h = S_{11}|_{f=0}^{p\to m} - S_{11}|_{f=0}^{m\to p} \quad \text{(or)} \quad h = S_{11}|_{f=1}^{p\to m} - S_{11}|_{f=1}^{m\to p},$$

we find that

$$h = \frac{2\sqrt{3}}{\gamma} D_0 \tag{54}$$

in both cases. Further, D_0 is a material constant, assumed to be independent of temperature. Hence, we find that the width of the hysteresis loop *as predicted by this model* remains constant for a given material system [see Müller and Xu (1991), for a similar conclusion with the width of the hysteresis loop based on Landau–Devonshire model]. Also note that h predicted by this model remains constant in general for proportional loading cases. However, note that the hysteresis loop is sensitive to partial transformations, and we shall return to this in the study of the thick cylinder.

4.2. *Material parameters*

Several material parameters have to be prescribed *a priori*. The following temperature independent material constants have to be specified: the transformation temperature θ_0, the martensite start temperature M_s, the strain constant γ, and the free energy constant k (14). The principal objective here is to simulate stress induced martensitic transformation, and model the stress–strain behavior at various temperatures above martensite start temperature ($\theta > M_s$). Note that the superelastic behavior becomes prominent at temperatures greater than austenite finish temperature ($\theta > A_f$). Therefore, at a given temperature θ, we need to specify the shear modulus $\mu(\theta)$ and the hardening parameter $H(\theta)$.

4.2.1. *Remark* 3. The shear modulus $\mu(\theta)$ as given in eqn (3) is actually the shear modulus of the inclusions (the martensite). Here, we assume that the differences in elastic moduli between the austenite and martensite phases are negligible.

The shear modulus variation with temperature can be approximated by a linear variation (Sun and Hwang, 1993; Reniecki and Lexcellent, 1994) as

$$\mu(\theta) = \begin{cases} q_1(\theta - M_s) + \mu_0, & \theta > M_s, \quad q_1 > 0 \\ q_2(\theta - M_s) + \mu_0, & \theta < M_s, \quad q_2 < 0 \end{cases} \tag{55}$$

4.2.2. *Remark* 4. Sun and Hwang (1993) use the transformation temperature θ_0 instead of M_s in the above linear approximation for the shear modulus. However, looking at the data reported in the literature, we observed that the root of the V-shaped $\mu(\theta)$ vs θ curve

is, in general, at M_s [see Hasiguti and Iwasaki (1968); Zirinsky (1956)]. Besides, the precise calculations for θ_0 is not always clear (Salzbrenner and Cohen, 1979).

The constant $B(\theta)$ is determined from the shear modulus using eqn (3). By using eqn (53), we can determine $H(\theta)$ from uniaxial stress–strain results from an experiment at a particular temperature. However, while the variation of $H(\theta)$ with temperature is not clear yet, the model has the provision to accommodate the variation. The numerical formulation can be modified easily to include any variation.

At $\theta = M_s$, the stress required to nucleate the transformation is in general zero [see Otsuka and Shimuzu (1986), p. 98, Fig. 10]. Hence, $C_f\ (M_s, f = 0) = 0$, and from this we can obtain the dissipation constant D_0 as

$$D_0 = \tfrac{1}{4}B(M_s)\gamma^2 - \Delta G(M_s) - H(M_s).$$

The transformation parameters $C_f(\theta)$ and $C_r(\theta)$ can be obtained from

$$C_f(\theta) = D_0 + \Delta G(\theta) + H(\theta) - \tfrac{1}{4}B(\theta)\gamma^2$$

$$C_r(\theta) = C_f(\theta) - 2D_0.$$

To summarize, the temperature independent constants that have to be specified are

$$\nu, \theta_0, M_s, \gamma, k, q_1, q_2, \mu_0,$$

and the temperature dependent material parameter that needs to be specified is the hardening parameter $H(\theta)$.

4.2.3. *Remark* 5. The temperature independent material parameters specified above can be obtained from uniaxial stress strain data from carefully conducted experiments at various temperatures. The equations given earlier can be easily manipulated with the experimental data to obtain the constants. Using experimental data from various temperatures provides an opportunity to test the validity of the model, since the constants estimated at different temperatures should be reasonably independent of temperature.

4.3. *Finite element discretization*

We study the uniaxial behavior using a 4-node linear quadrilateral, isoparametric element [see Reddy (1993)]. The mesh consists of a single element, with axisymmetric boundary conditions (see Fig. 2). Each Gauss point in an element is associated with a

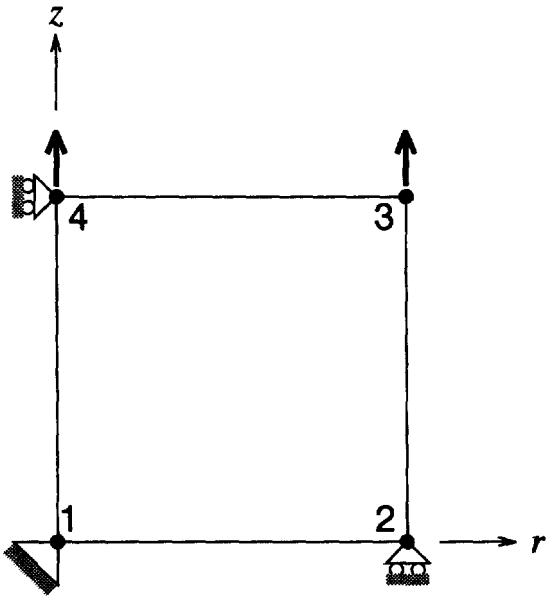

Fig. 2. Single element finite element mesh with axisymmetric boundary conditions.

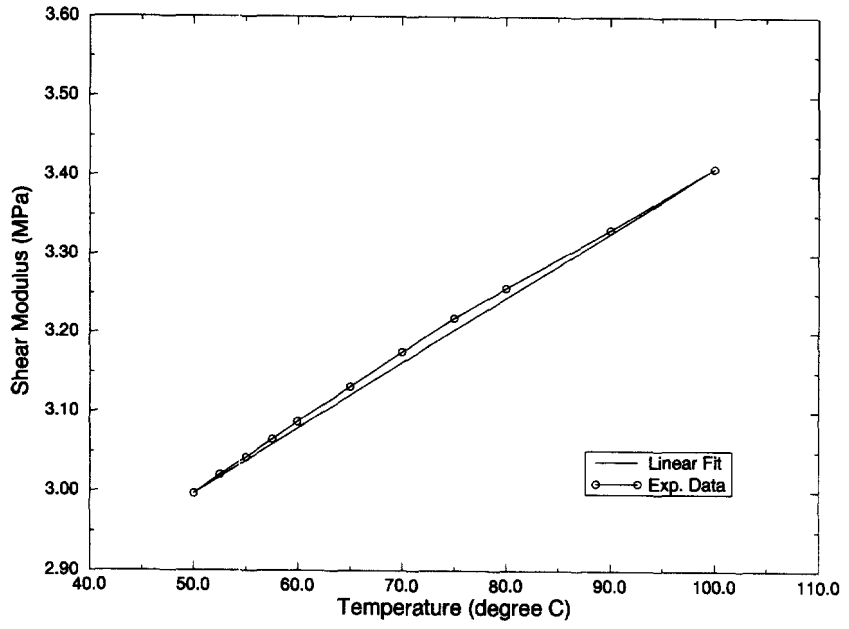

Fig. 3. The variation of $\mu(T)$ with temperature in the range of 50–100°C (Zirinsky, 1956), and its linear approximation.

representative volume element. The internal variables (f, ε^p), and other variables $(\mathbf{S}, \mathbf{E}, \sigma)$ get updated at each Gauss point. Note that unlike the elastoplastic problem, which is characterized by complete elastic unloading, the superelastic behavior of SMAs is characterized by a reverse transformation phase, akin to a reverse yield surface.

4.4. *Gold–cadmium alloy (Au-47.5at%Cd)*

Warlimont and Delaey (1974) provide an extensive review of noble metal based alloys that undergo reversible martensitic transformations. The gold–cadmium alloy (Au47.5at%Cd) undergoes a phase transformation from BCC (β_2, austenite) to orthorhombic $2H$ (γ_2', martensite). Zirinsky (1956) was perhaps the first to provide experimental data on temperature dependence of elastic compliances for Au-47.5at%Cd alloy. The martensite start temperature (M_s) reported in his study is 50°C (though Zirinsky defines this to be the transformation temperature). The elastic shear modulus shows a monotonic increase from 50°C (see Fig. 3). Looking at the literature, we find a wide range of reported values for M_s and A_s for the same alloy system. Table 3 summarizes some of the data from the literature for Au-47.5at%Cd.

We will follow Nakanishi *et al.* (1973), and choose the following transformation temperature values

$$M_s = 58°C, \quad A_s = 72°C, \quad \theta_0 = 65°C.$$

Further, from Zirinsky (1956) (see Fig. 3), we obtain $q_1 = 8.24$ MPa/°C. While the transformation temperatures are different between Nakanishi *et al.* (1973) and Zirinsky (1956),

Table 3. Transformation temperatures for Au-47.5at%Cd reported in literature

Reference	M_s (°C)	A_s (°C)	Crystal type	Experimental method
1. Zirinsky (1956)	50	72	Single	Thermocouple with composite oscillator
2. Nakanishi *et al.* (1973)	58	72	Single	Differential scanning calorimeter
3. Sakamoto and Shimizu (1982)	55		Single	Not measured—extrapolated
4. Baram and Rosen (1981)	55	67.5	Polycrystal	Acoustic emission
5. Baram and Rosen (1982)	62.5	67.5	Polycrystal	Acoustic emission
	60	72	Polycrystal	Electrical resistivity

we assume here that the rate of change of shear modulus with temperature does not vary significantly between their experiments. The other temperature independent material constants are

$$\nu = 0.25, \quad k = 0.1112 \text{ MPa } ^\circ C^{-1}, \quad \gamma = 0.0452, \quad D_0 = 0.416 \text{ MJ m}^{-3}.$$

The hardening parameter $H(\theta)$ is chosen to be a constant and not vary with temperature, and is set equal to -1.876 MJ m^{-3}. The other temperature dependent parameters are obtained as outlined in Section 4.2, and are given in Table 4.

At this juncture, it is important to mention an inconsistency in our modeling. The material used for study in Nakanishi *et al.* (1973) is a single crystal, and hence, possesses a distinct symmetry. However, the present formulation assumes material isotropy, and is consequently appropriate for polycrystals. Despite this obvious inconsistency, we have gone ahead and modeled Au-47.5at%Cd because of lack of good data on polycrystalline specimens of this material. Of course, the present formulation can be modified to model correct symmetries. However, the orientation of single crystals with respect to the tensile axis of the experiment is critical, and hence, this aspect should also be built into a successful model.

Nakanishi *et al.* (1973) reported the stress–strain curve at $\theta = 84^\circ$C (see Fig. 1 in their paper) and, hence, this temperature has also been included in the simulation here. The analytical solution and finite element results are shown in Fig. 4, and as is evident, the results agree well. Qualitative agreements with the experimental values reported by Nakanishi *et al.* (1973) are good. However, quantitative agreements are not very good because of the fact that the hardening in Nakanishi *et al.* (1973) is not linear in the early stages of the transformation and during the beginning of the reverse transformation. Also, as derived earlier (54), the width of the hysteresis loop, is equal to 31.88 MPa, and the numerical results predict the same value. Note that this predicted value of hysteresis is nearly equal to the hysteresis value measured from the experiment at $\theta = 84^\circ$C (Nakanishi *et al.*, 1973).

4.5. *Titanium–nickel alloy (Ti-50.6at%Ni)*

The commercially most popular shape memory alloys are Ti–Ni alloys. The large popularity is in large measure due to the large recoverable strains in these alloy systems, both in single crystal form and polycrystalline forms (Bhattacharya and Kohn, 1995). The alloy undergoes a BCC (β_2) to monoclinic transformation. A large amount of experimental data is available on nearly equi-atomic Ti–Ni alloys. The composition varies slightly between the reported results (Ni content varies by few tenths of a percent). While this does not affect the mechanical properties in general, it does affect the transformation temperatures greatly (Lindgård, 1994; Hasiguti and Iwasaki, 1968).

Table 5 summarizes some of the experimental data on Ti–Ni alloys (the composition varies between the references). For our simulation here, we have adopted the data reported by Miyazaki *et al.* (1981). As given in the table, the transformation temperature values for this Ti-50.6at%Ni alloy are

$$M_f = 128 \text{ K}, \quad M_s = 190 \text{ K}, \quad A_s = 188 \text{ K}, \quad A_f = 221 \text{ K}.$$

Again, with the assumption that except the transformation temperature, other material

Table 4. Material parameters for Au-47.5at%Cd

θ (°C)	$\mu(\theta)$ (MPa)	$B(\theta)$ (MPa)	$C_f(\theta)$ (MJ m^{-3})	$C_r(\theta)$ (MJ m^{-3})
65	2263.24	−2313.53	0.17	−0.66
75	2345.64	−2397.77	1.33	0.50
84	2419.80	−2473.57	2.37	1.54
85	2428.04	−2482.00	2.48	1.65
95	2510.44	−2566.23	3.64	2.81

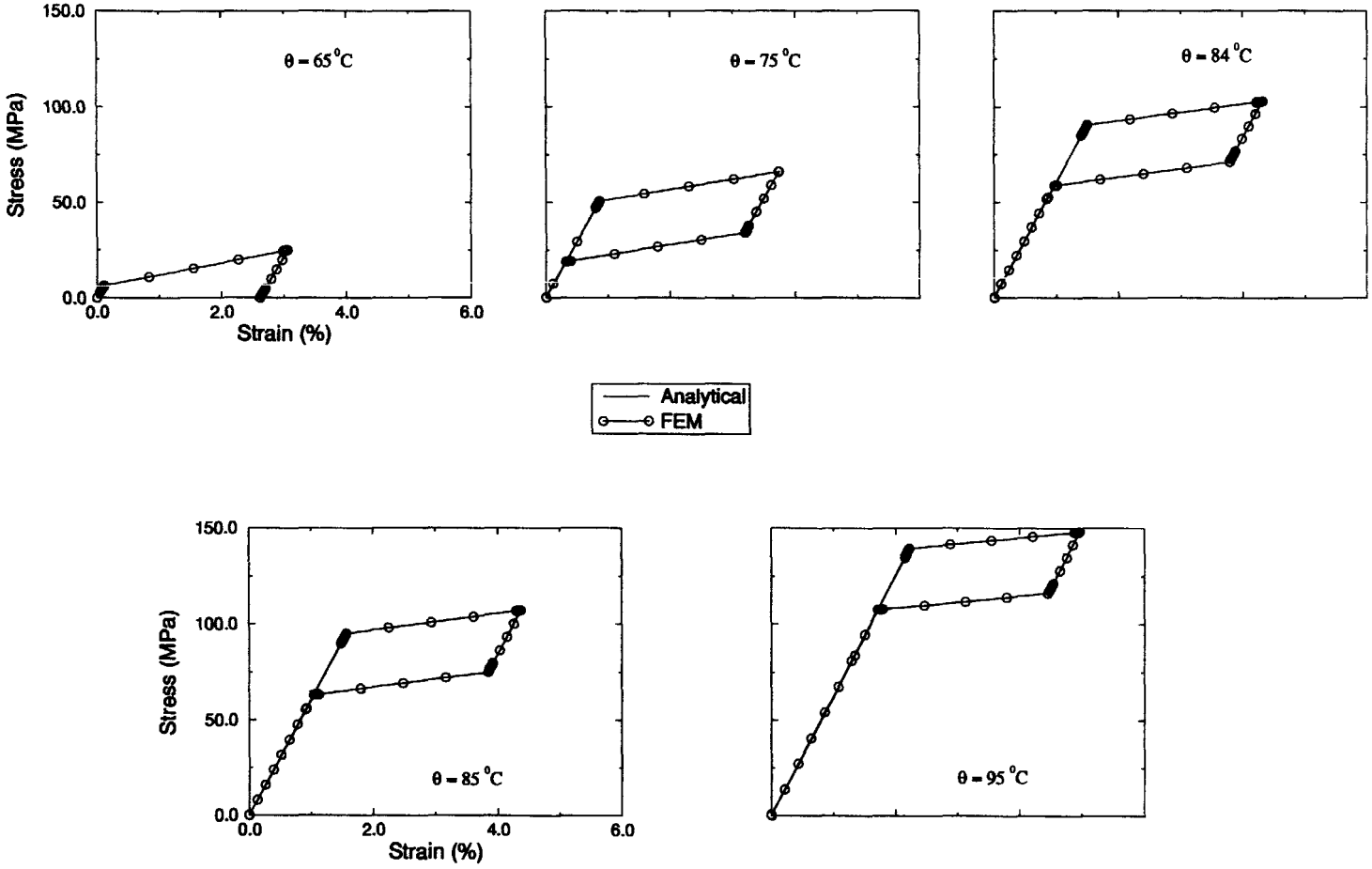

Fig. 4. Stress–strain curves at various temperatures for Au-47.5at%Cd.

Table 5. Transformation temperatures for Ti–Ni reported in literature

Reference	M_s (K)	A_s (K)	Crystal type
1. Hasiguti and Iwasaki (1968)	313		Ti-51.0at%Ni, Single crystal
2. Miyazaki *et al.* (1981)	190	188	Ti-50.6at%Ni, Polycrystal
3. Saburi *et al.* (1982)	282		Ti-50.4at%Ni, Polycrystal
	265		Ti-50.7at%Ni, Polycrystal
	257		Ti-51.0at%Ni, Polycrystal
4. Shaw and Kyriakides (1995)	272	302.5	Ti-50.1at%Ni, Polycrystal

properties are not significantly affected by minor compositional variations, we adopt the shear modulus variations reported by Hasiguti and Iwasaki (1968)† (for Ti-51at%Ni, $M_s = 40°C$). From their curves, we can infer $q_1 = 5.8$ MPa K^{-1}, $q_2 = -17.4$ MPa K^{-1} [see also Sun and Hwang (1993)]. The other temperature independent material constants are

$$\nu = 0.25, \quad k = 0.2084 \text{ MPa K}^{-1}, \quad \gamma = 0.0554, \quad D_0 = 2.3988 \text{ MJ m}^{-3}.$$

The hardening parameter $H(\theta)$ is once again assumed to be a constant and equal to -6.9227 MJ m^{-3}. The other temperature dependent parameters are tabulated in Table 6.

Miyazaki *et al.* (1981) reported the stress–strain curves at various temperatures (see Fig. 1 in their paper). The analytical and numerical results of the present formulation are shown in Fig. 5, and once again, these agree well. In this case, the agreements between the experimental values and the values calculated from the model are good both qualitatively and quantitatively, and the reason can be attributed to the linear hardening behavior evident in the experimental stress–strain curves (Miyazaki *et al.*, 1981). The width of the hysteresis loop, as calculated from eqn (54) is 150 MPa, and the numerical results predict the same value. Again, the predicted value is approximately equal to the experimentally measured values in the superelastic regime ($\theta = 225$–245 K).

4.6. *Thick cylinder*

Most of the experiments on shape memory behavior have been performed using either drawn wires (polycrystals) or small rectangular specimens (single crystals). Uniaxial experiments on such specimens result in an inhomogeneous stress response due to imperfections and presence of grips (in fact, martensite fronts are observed to initiate at the ends near the grips and propagate inward). Also, a displacement controlled loading program often does not generate a uniaxial stress state. However, in numerical simulations, uniaxial loading results in a homogeneous stress state, and hence, all the RVEs in the entire length of the material transform simultaneously. This requires the introduction of some imperfections (geometric) to trigger inhomogeneity in the stress response, so that the usually observed behavior of martensitic fronts starting at the grips and moving inward can be modeled. Instead of introducing imperfections in a model of a wire, we decided to model a different problem: a classical problem in elastoplasticity that provided the inhomogeneous response and promised some interesting behavior.

Table 6. Material parameters for Ti-50.6at%Ni

θ (°K)	$\mu(\theta)$ (MPa)	$B(\theta)$ (MPa)	$C_f(\theta)$ (MJ m^{-3})	$C_r(\theta)$ (MJ m^{-3})
205	8362.63	−8548.47	1.93	−2.87
215	8420.63	−8607.76	4.06	−0.74
225	8478.63	−8667.04	6.19	1.39
235	8536.63	−8726.33	8.32	3.52
241	8571.43	−8761.91	9.60	4.80
245	8594.63	−8785.62	10.45	5.65

† Actually, Hasiguti and Iwasaki (1968) report the variation of period of a torsion pendulum, T with temperature. The period of vibration is proportional to shear modulus ($T \propto \mu^{-1/2}$).

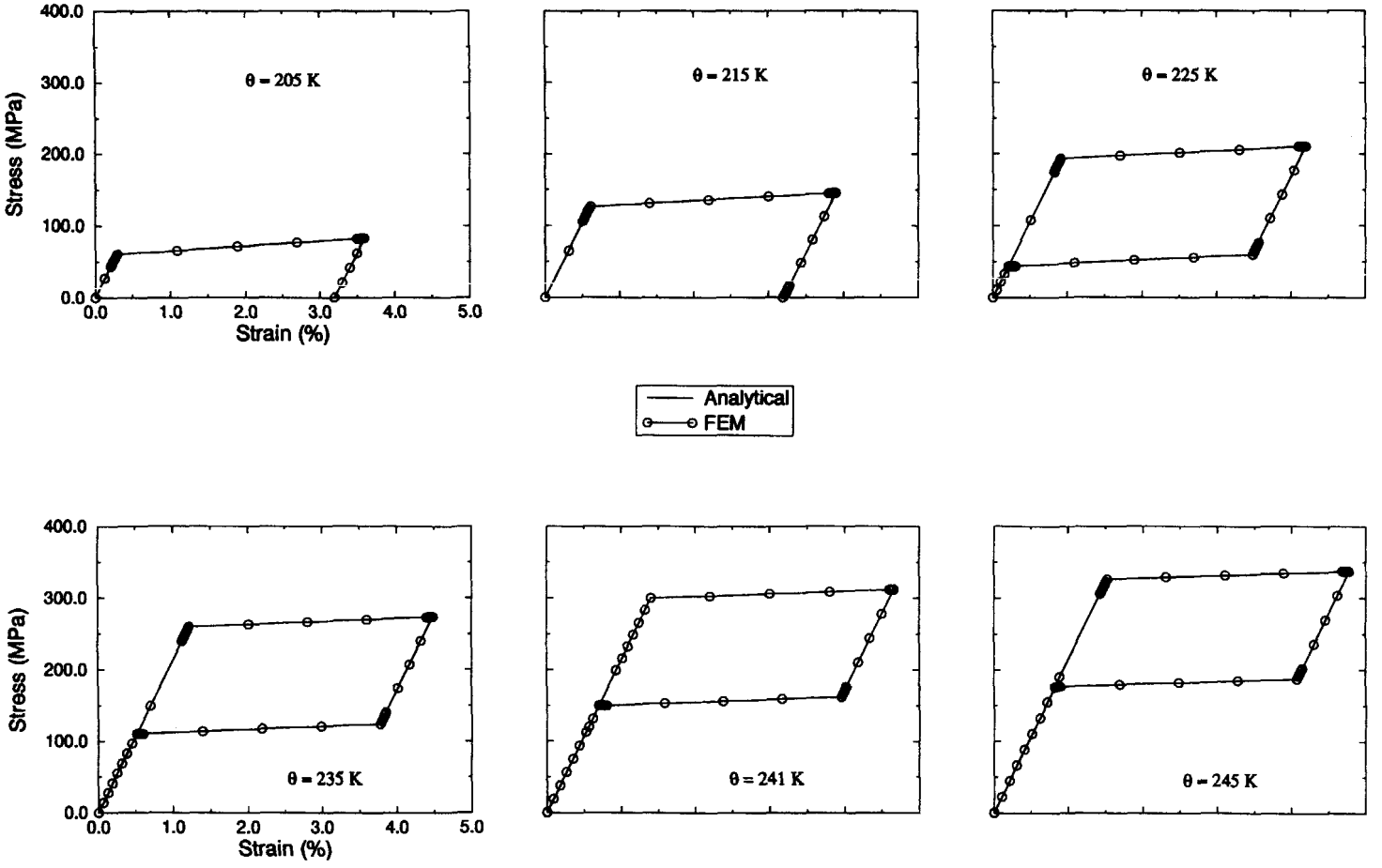

Fig. 5. Stress–strain curves at various temperatures for Ti-50.6at%Ni.

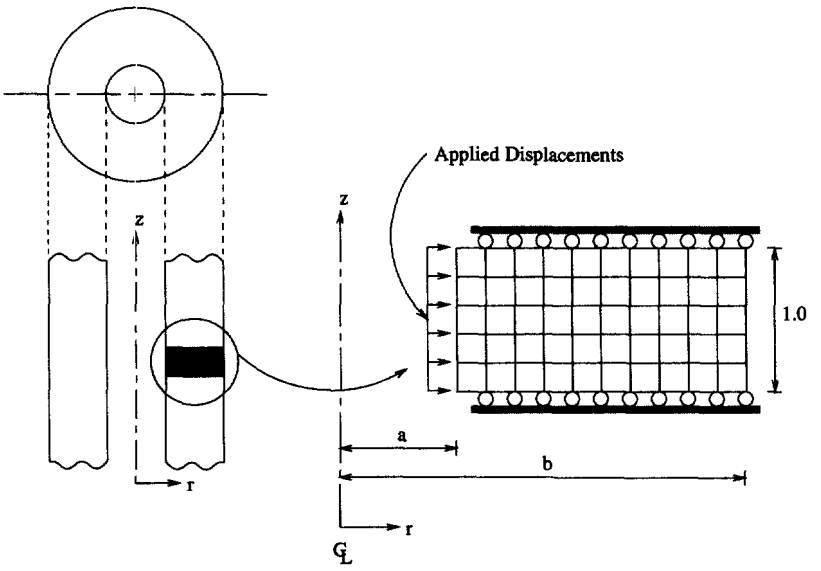

Fig. 6. Geometry and the finite element mesh of an axisymmetric model of a thick cylinder ($b/a = 2.0$).

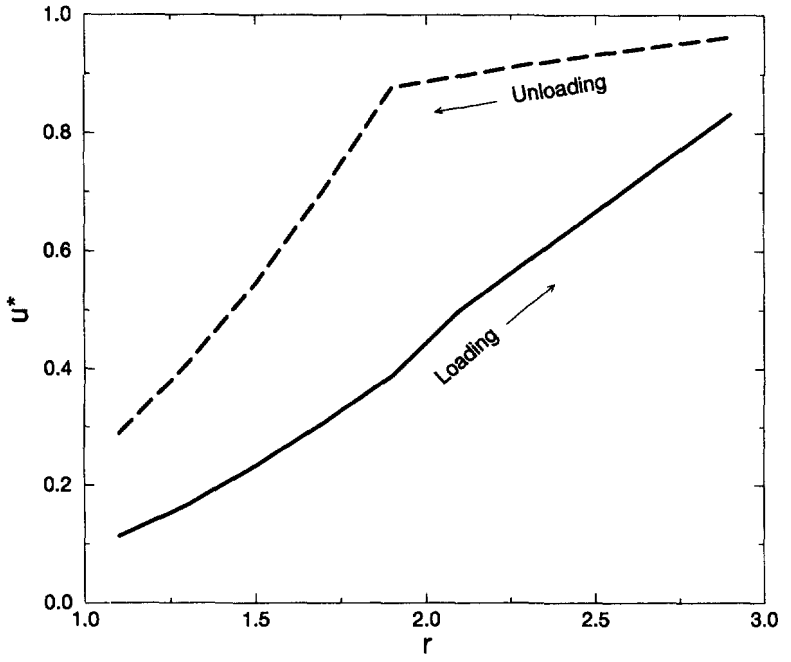

Fig. 7. Applied displacements (at $r = a$) at which the first martensite plate appears across the cylinder (along r).

The problem involved an infinitely long thick cylinder subjected to internal pressure. An axisymmetric model of the cylinder was used, and only a unit length in the axial direction of the cylinder was modeled (periodic boundary conditions were imposed on the top and bottom sides). The geometry and the mesh are shown in Fig. 6. Displacements (u^*) were applied at the internal side. The material properties defined for Au-47.5at%Cd previously at $\theta = 84°C$ were used.

The applied displacements (at the internal end, $r = a$) at which the first martensite plate appears during loading and disappears during unloading at locations across the cylinder (along r) are shown in Fig. 7. While the loading curve is almost linear, the unloading curve exhibits some interesting behavior. The locations near the right end of the cylinder that transformed last are quick to revert back to the parent phase as is expected. However,

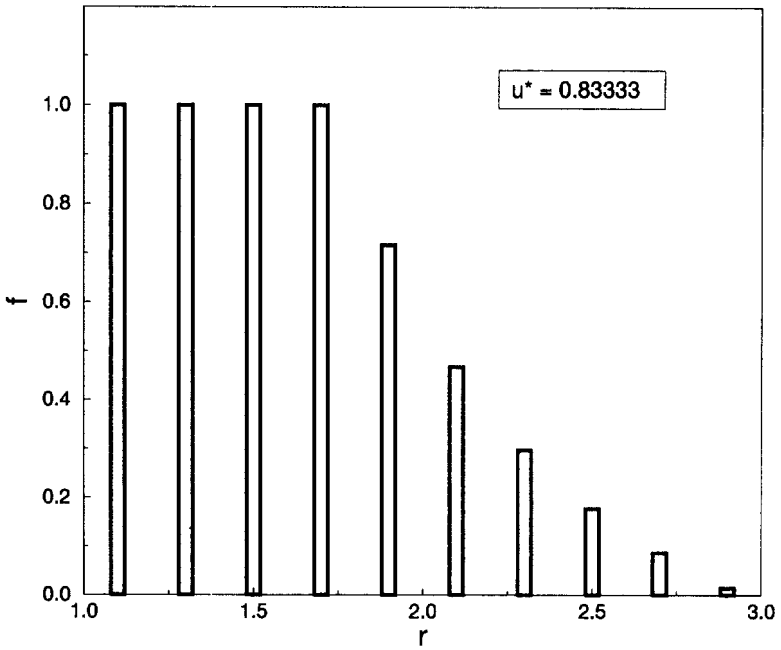

Fig. 8. Martensite volume fraction distribution across the cylinder at a particular value of applied displacement ($u^* = 0.83333$).

we see a distinct change of slope during unloading. The reason for this behavior is the following. Martensite is nucleated at the outer end of the cylinder under high loads ($u^* \sim 0.8$). However, by the time this load is reached, the inner end of the cylinder is fully transformed, and is in elastic regime (of martensite†), and hence, has to unload significantly before it can revert back to the parent phase.

This is further highlighted in Fig. 8 which is a snapshot of the variation of martensite volume fraction across the cylinder at a particular value of applied displacement (actually this value corresponds to the rightmost point in the loading curve of Fig. 7). As is clear from the figure, the first four Gauss points have transformed fully, while only the first martensite plate is nucleated at the outer end.

Figures 9 and 10 show the variation of radial stress (S_{rr}) and the hoop stress ($S_{\theta\theta}$) across the cylinder at various values of r^*. The normalized value ($r^* = r/a$) corresponds to the location of martensite 'front'‡ plate during loading. The distributions of both the stresses are similar to the behavior in elastoplasticity [see Lubliner (1990), p. 255]. However, there is one difference that distinguishes the shape memory behavior. In Figs 9 and 10, the dashed line shows the stress distribution at the time (loading) at which the first martensite plate appears at the outer end of the cylinder. In Fig. 10, the behavior at the inner end of the cylinder at this time ($r^* = 1.9$) is different from the previous cases ($r^* = 1.7$ and below). The reason is again the same: the inner end is back into elastic response regime, and hence, has a higher stress. The peaks in the hoop stress (Fig. 10) correspond to a balance between the load carried by the austenite and martensite. The martensite volume fraction decreases from left to right in Fig. 10 (with increasing r). The low hoop stresses to the left of the peak correspond to higher martensite volume fraction, and the low hoop stresses to the right of the peak correspond to the fact that these regions are still in the lower stages of the loading program, and hence, have lower stresses.

As per our original formulation, under partial transformation, say to point p in Fig. 11, the reverse transformation will begin at q. Instead, it has been observed in some experiments (Müller and Xu, 1991; Fu *et al.*, 1992) that the reverse transformation actually

† The elasticities of both the phases (while homogeneous) are assumed to be the same. This is usually not the case, but the difference in elasticities can be accommodated within our approach easily.

‡ The martensite front actually corresponds to the appearance of the first martensite plate across the cylinder (compare with Fig. 6).

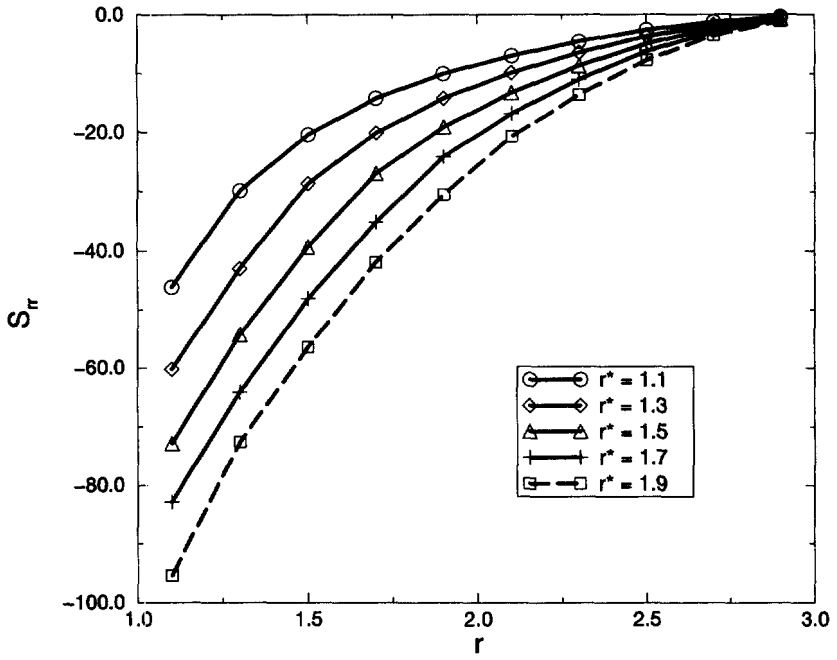

Fig. 9. Distribution of radial stresses across the cylinder as the martensite 'front' (appearance of first martensite plate) traverses the radius of the cylinder.

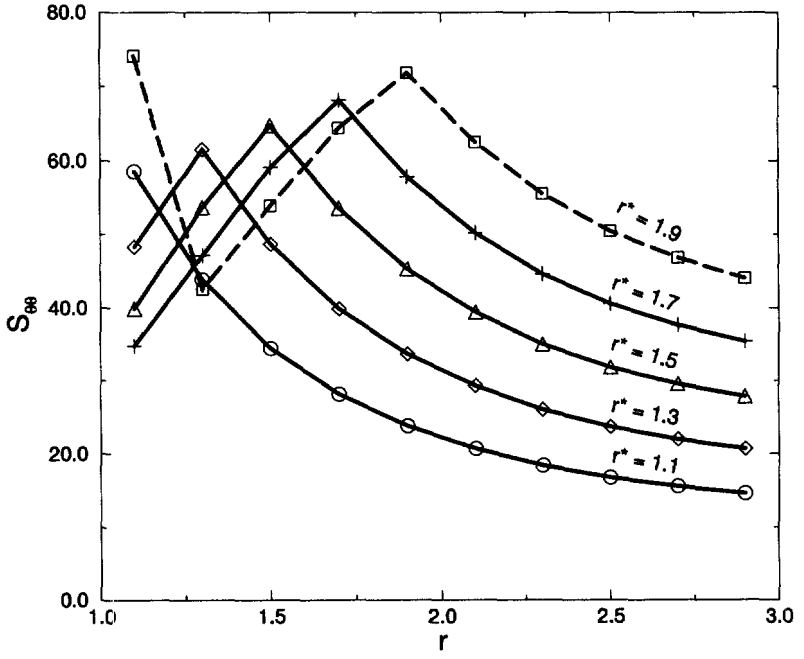

Fig. 10. Distribution of hoop stresses across the cylinder as the martensite 'front' (appearance of first martensite plate) traverses the radius of the cylinder.

begins at point r in Fig. 11 corresponding to a partial transformation up to point p. In order to capture this behavior, we modify the parameter $C_r(\theta,f)$ in eqn (21) to

$$C_r(\theta,f) = C_f(\theta,f) - 2fD_0. \tag{56}$$

The introduction of f into the equation allows the variation of dissipation with the amount of transformation. Indeed, Fig. 12 shows the stress–strain diagram for the thick cylinder

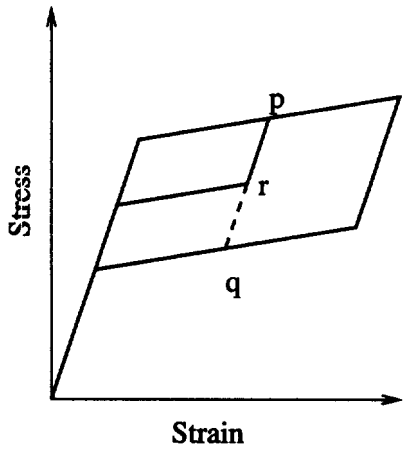

Fig. 11. An idealized stress–strain curve with a subloop due to partial transformation.

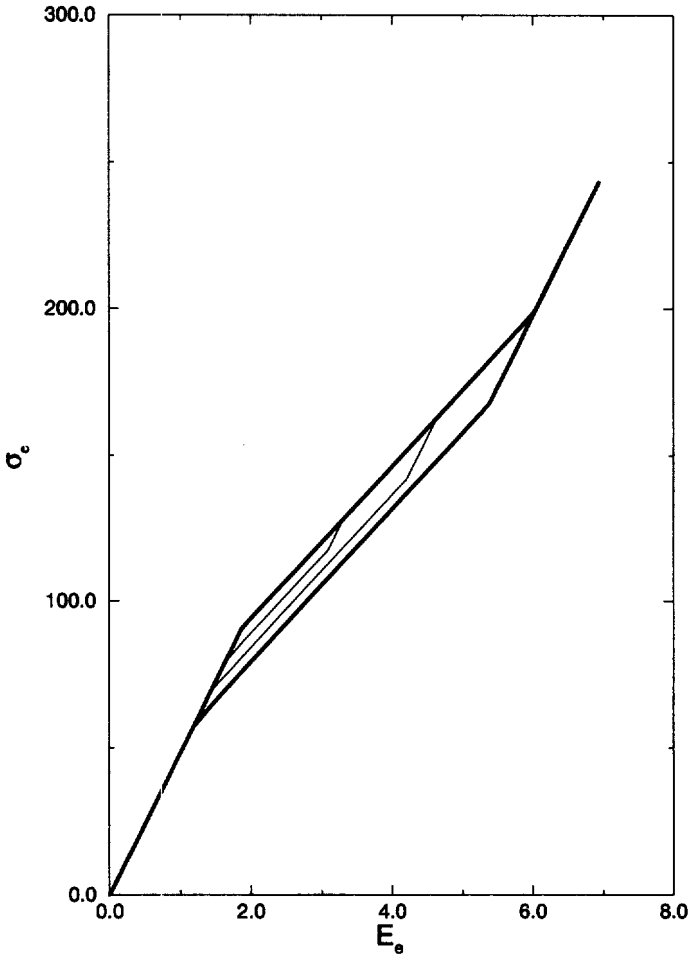

Fig. 12. Stress–strain curves with subloops due to partial transformation.

problem near the inner end of the cylinder. We have plotted the equivalent stress (σ_e) against the equivalent strain (E_e), where

$$E_e = (\tfrac{3}{2}\mathbf{E}\cdot\mathbf{E})^{1/2}.$$

Two subloops are shown in the figure that correspond to partial transformations. While

this demonstrates that the subloops can be included in the model without modifying the existing framework, the nature of the subloops in the material behavior is far from clear [see Tanaka *et al.* (1995)].

5. CLOSURE

We have presented a finite element formulation of a micromechanics based constitutive model for shape memory alloys, and have validated the finite element formulation with numerical results for two alloy systems (Au-47.5at%Cd and Ti-50.6at%Ni), and studied a thick cylinder problem. The purpose here was to demonstrate the inclusion of SMA constitutive model in a conventional elastoplastic finite element code. A particular model was chosen as it represented a class of such models, and the model itself was derived on strict thermodynamic principles. The formulation presented here provides a testbed approach to study and evaluate several constitutive models, and we have indicated the similarity of the model presented here to similar class of models.

The focus of the present study was on stress induced martensitic transformations, and reorientation effects were not considered. However, numerical formulations of reorientation is rather straight-forward in the framework presented here.

In our attempt to obtain realistic experimental data for simulation, we observed that the literature in fact has a wealth of information, and there are similarities in results reported. However, due to factors such as sensitivity to composition, processing technique, aging, crystalline form, grain size, anisotropy ratio, texture, etc., there are differences in reported results that limits the usefulness of these results as excellent bench marks. Careful experimentations on alloys systems representative of various change of symmetries (BCC to tetragonal, orthorhombic, and monoclinic), both in single crystal and polycrystalline forms, with calorimetric measurements, are necessary to successfully test the constitutive models. While such experiments have in fact been performed for some alloy systems by Miyazaki and co-workers (Miyazaki *et al.*, 1981, Miyazaki and Ohtsuka, 1987) and more recently by Shaw and Kyriakides (1995), more experimental data are necessary. A numerical formulation of the constitutive models, such as the one presented here, provides a common base on which several models can be evaluated, and compared with rigorous experimental results.

Acknowledgements—This work was partially supported by the Army Research Office through the grant DAAH 04-96-1-0080.

REFERENCES

Abeyaratne, R., Kim, S. and Knowles, J. K. (1994) A one-dimensional continuum model for shape-memory alloys. *International Journal of Solids and Structures* **31,** 2229–2249.

Abeyaratne, R., Chu, C. and James, R. (1995) Kinetics of materials with wiggly energies: theory and application to the evolution of twinning microstructures in a Cu–Al–Ni shape memory alloy. Preprint.

Ball, J. M. and James, R. (1987) Fine phase mixtures as minimizers of energy. *Archives of Rational Mechanical Analysis* **100,** 13–52.

Ball, J. M. and James, R. (1992) Proposed experimental tests of a theory of fine microstructure and the two-well problem. *Philosophical Transactions of the Royal Society of London A* **338,** 389–450.

Baram, J. and Rosen, M. (1982) On the nature of the thermoelastic martensitic phase transformation in Au-47.5at%Cd determined by acoustic emission. *Acta Metallica* **30,** 655–662.

Bhattacharya, K. and Kohn, R. V. (1996) Symmetry, texture and the recoverable strain of shape memory polycrystals. *Acta Metallica* **44,** 529–542.

Bo, Z. and Lagoudas, D. C. (1994) A unified thermodynamic constitutive model for SMA and its implementation to a finite element analysis. In *Recent Advances in Engineering Science, Proceedings of the* 31*st Annual Technical Meeting of the Society of Engineering Science*, Texas A & M University, College Station, TX.

Boyd, J. G. and Lagoudas, D. C. (1996) A thermodynamic constitutive model for shape memory materials. Part I. The monolithic shape memory alloy. *International Journal of Plasticity* **12,** 805–842.

Brinson, L. C. and Lammering, R. (1993) Finite element analysis of the behavior of shape memory alloys and their applications. *International of Solids and Structures* **30,** 3261–3280.

Fischer, F. D., Berveiller, M., Tanaka, K. and Oberaigner, E. R. (1994) Continuum mechanical aspects of phase transformations in solids. *Archives of Applied Mechanics* **64,** 54–85.

Fu, S., Müller, I. and Xu, H. (1992) On the thermodynamics of pseudoelasticity. *Proceedings of the International Conference on Martensitic Transformations*, Monterey, CA, pp. 335–340.

Funakubo, H. (ed.) (1987) *Shape Memory Alloys*. Gordon and Breach, New York.

Gurtin, M. (1981) *An Introduction of Continuum Mechanics*. Academic Press, San Diego, CA.
Hasiguti, R. R. and Iwasaki, K. (1968) Internal friction and related properties of the TiNi intermetallic compound. *Journal of Applied Physics* **39,** 2182–2186.
Khachaturyan, A. G. (1983) *Theory of Structural Transformations in Solids*. Wiley, New York.
Krishnakumar, R., Rengarajan, G. and Reddy, J. N. (1995) Finite element analysis of pseudoelastic behavior of shape memory alloys using a micromechanics based constitutive model. In *Recent Advances in Composite Materials Research*, MD-Vol. 56, ed. S. R. White *et al.*, 1995 Joint ASME Applied Mechanics and Materials Summer Meeting. UCLA, Los Angeles, CA, pp. 203–214.
Lindgård, P. A. (1994) What determines the martensitic temperature in alloys? In *Journal de Physique, III European Symposium on Martensitic Transformations, ESOMAT '94*, ed. A. Planes *et al.*, Barcelona, Spain, Vol. **5**(C2), pp. 29–33.
Lubliner, J. (1981) *Plasticity Theory*. Macmillan, New York.
Miyazaki, S. and Otsuka, K. (1987) Copper-based shape memory alloys. In *Shape Memory Alloys*, ed. H. Funakubo. Gordon and Breach, New York.
Miyazaki, S., Otsuka, K. and Suzuki, Y. (1981) Transformation pseudoelasticity and deformation behavior in a Ti-50.6at%Ni alloy. *Scripta Metallica* **15,** 287–292.
Mori, T. and Tanaka, K. (1973) Average stress in matrix and average elastic energy of materials with misfitting inclusions. *Acta Metallica* **21,** 571–574.
Müller, I. (1994) Thermodynamics of ideal pseudoelasticity. In *Journal de Physique, III European Symposium on Martensitic Transformations, ESOMAT '94*, ed. A. Planes *et al.*, Barcelona, Spain, Vol. **5**(C2), pp. 423–431.
Müller, I. and Xu, H. (1991) On the pseudo-elastic hysteresis. *Acta Metallica Materiala* **39,** 263–271.
Nakanishi, N., Mori, T., Miura, S., Murakami, Y. and Kachi, S. (1973) Pseudoelasticity in Au–Cd thermoelastic martensite. *Philosophical Magazine* **28,** 277–292.
Ortin, J. and Planes, A. (1988) Thermodynamic analysis of thermal measurements in thermoelastic martensitic transformations. *Acta Metallurgica* **36,** 1873–1889.
Ortiz, M. and Simo, J. C. (1986) An analysis of a new class of integration algorithms for elastoplastic constitutive relations. *International Journal of Numerical Methods of Engineering* **23,** 353–366.
Otsuka, K. and Shimuzu, K. (1986) Pseudoelasticity and shape memory effect in alloys. *International Metals Review* **31,** 93–114.
Patoor, E., Eberhardt, A. and Berveiller, M. (1988) Thermomechanical behavior of shape memory alloys. *Archive Mechanics* **40,** 775–794.
Patoor, E., Eberhardt, A. and Berveiller, M. (1994) Micromechanical modelling of the superelastic behaviour. In *Journal de Physique, III European Symposium on Martensitic Transformations, ESOMAT '94*, ed. A. Planes *et al.*, Barcelona, Spain, Vol. 5(C2), pp. 501–506.
Raniecki, B. and Lexcellent, C. (1994) R_L-models of pseudoelasticity and their specification for shape memory solids. *European Journal of Mechanics, A/Solids* **13,** 21–50.
Reddy, J. N. (1993) *An Introduction to the Finite Element Method*, 2nd edn. McGraw-Hill, New York.
Rice, J. R. (1971) Inelastic constitutive relations for solids: An internal-variable theory and its application to metal plasticity. *Journal of Mechanics and Physics of Solids* **19,** 433–455.
Salzbrenner, R. J. and Cohen, M. (1979) On the thermodynamics of thermoelastic martensitic transformations. *Acta Metallica* **27,** 739–748.
Shaw, J. A. and Kyriakides, S. (1995) Thermomechanical aspects of NiTi. *Journal of Mechanics and Physics of Solids* **43,** 1243–1281.
Simo, J. C. and Hughes, T. J. R. (1988) *Elastoplasticity and Viscoplasticity: Computational Aspects*. Stanford University, CA.
Sun, Q. P. and Hwang, K. C. (1993) Micromechanics modelling for the constitutive behavior of polycrystalline shape memory alloys—I. Derivation of general relations. *Journal of Mechanics and Physics of Solids* **41,** 1–17; II. Study of the individual phenomena. *Journal of Mechanics and Physics of Solids* **41,** 19–33.
Sun, Q. P., Leclercq, S. and Lexcellent, C. (1994) A micromechanics constitutive model of shape memory alloy single crystal with internal hysteresis loops. Preprint.
Tanaka, K. (1986) A thermomechanical sketch of shape memory effect: one-dimensional tensile behavior. *Research Mechanica* **18,** 251–263.
Tanaka, K., Nishimura, F. and Tobushi, H. (1995) Transformation start lines in TiNi and Fe-based shape memory alloys after incomplete transformations induced by mechanical and/or thermal loads. *Mechanical Material* **19,** 271–280.
van Midden, H. (1994) Phase transformations in NiTi and Ti; an atomistic approach. Ph.D. Dissertation, University of Twente, The Netherlands.
Warlimont, H. and Delaey, L. (1974) Martensitic transformation in copper- silver- and gold-based alloys. *Progress in Materials Science* **18,** 1–147.
Wayman, C. M. (1964) *Introduction of Crystallography of Martensitic Transformation*. Macmillan, New York.
Wechsler, M. S., Lieberman, D. S. and Read, T. A. (1953) On the theory of the formation of martensite. *Transactions of the AIME* **197,** 1503–1515.
Wollants, P., Roos, J. R. and Delaey, L. (1993) Thermally- and stress-induced thermoelastic martensitic transformations in the reference frame of equilibrium thermodynamics. *Progress in Material Science* **3,** 227–288.
Ziegler, H. and Wehrli, C. (1987) The derivation of constitutive relations from the free energy and the dissipation function. *Advances in Applied Mechanics* **25,** 183–238.
Zirinsky, S. (1956) The temperature dependence of the elastic constants of gold–cadmium alloys. *Acta Metallica* **4,** 164–171.